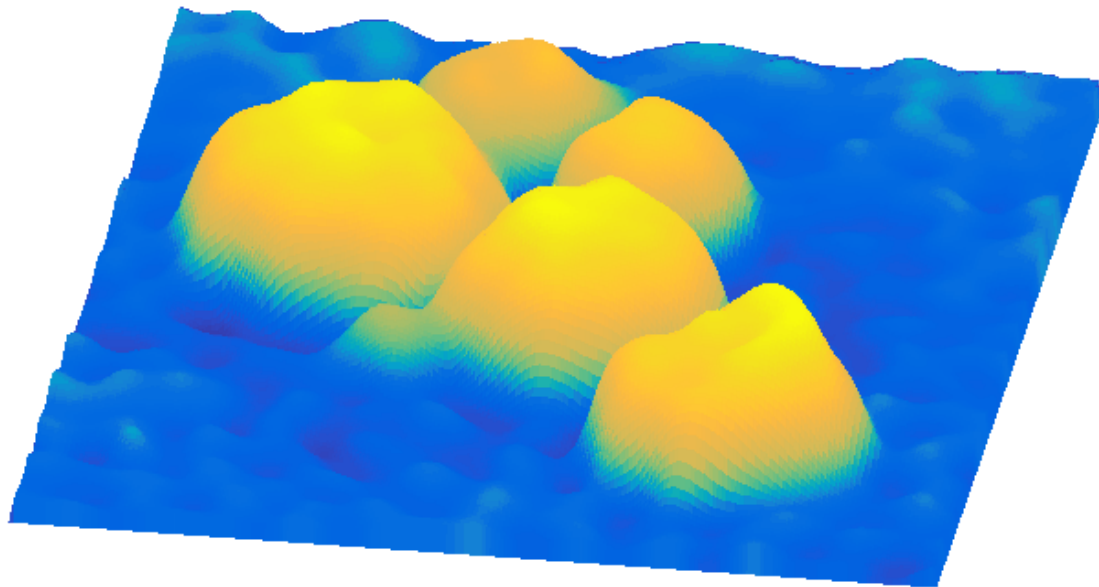




CHALMERS
UNIVERSITY OF TECHNOLOGY



Contactless noninvasive probing of model cells

Master's thesis in Nanotechnology

ARVID SKARRIE

MASTER'S THESIS 2017

Contactless noninvasive probing of model cells

ARVID SKARRIE



CHALMERS
UNIVERSITY OF TECHNOLOGY

Department of Chemistry and Chemical Engineering
CHALMERS UNIVERSITY OF TECHNOLOGY
Gothenburg, Sweden 2017

Contactless noninvasive probing of model cells
ARVID SKARRIE

© ARVID SKARRIE, 2017

Supervisor: Gavin Jeffries, Department of Chemistry and Chemical Engineering
Examiner: Aldo Jesorka, Department of Chemistry and Chemical Engineering

Master's Thesis 2017
Department of Chemistry and Chemical Engineering
Chalmers University of Technology
SE-412 96 Gothenburg
Telephone +46 31 772 1000

Cover: Visualization of a colony of yeast cells, computed from the phase difference generated by light passing through the yeast cells.

Contactless noninvasive probing of model cells
ARVID SKARRIE
Department of Chemistry and Chemical Engineering
Chalmers University of Technology

Abstract

This thesis covers three cases of contactless noninvasive probing of yeast cells and model cells; exploring different ways of characterizing the cell, without any sort of labelling. This enables studying single cells for a longer time period without affecting the cell's native behaviour.

A digital holography microscope records the interference pattern between two laser beams. By transforming this pattern, the sample can be visualized as a map over the phase differences, created by differences in refractive index of the sample and its environment. By comparing the phase differences for yeast cells in two different mediums, the geometry and refractive index of the cells in the sample can be determined. The refractive index for five yeast cells were determined to values between $n = 1.392 - 1.414$.

The same type of cells were also observed in an optical trapping microscope. By tightly focusing a laser beam, a yeast cell was trapped in the beam waist. They were easily manipulated and positioned in three dimension. The trapping force for $3.6 \mu\text{m}$ yeast cells were determined to $2.6 \mu\text{N m}^{-1}$.

Model cells in the form of giant unilamellar vesicles, GUVs, containing 5 % biotin, were bonded to streptavidin-coated $2.0 \mu\text{m}$ beads and as a way of probing the surface tension, membrane tethers were pulled out from a GUV. The force needed for tether formation and tether extension were determined for different pulling velocities; a maximum force of 1.8 pN was measured. The trapping strength were measured to $32.7 \mu\text{N/m}$.

Keywords: optical trap, optical trapping microscope, yeast cells, digital holographic microscope, giant unilamellar vesicles, noninvasive probing, model cell, trapping strength, vesicle tethers.

Acknowledgements

This project could not have been done without the help from the lovely people at the biophysical lab at Chalmers. First and foremost thanks to Gavin Jeffries for all the ideas, inspiration and supervision. Thanks to Daniel Midtvedt for the invaluable help with the DHM and yeast cells. Thanks to Bella Doosti and Vladimir Kirejev for teaching me the art of creating and befriending vesicles. Thanks to Aldo Jesorka for the opportunity of writing my thesis at the biophysical lab. Thanks to my office mates Astrid Olivefors and Barbora Spodniakova for not always being there before me.

Thanks to the rest of the people at the biophysical lab for all the help, knowledge and fika.

Arvid Skarrie, Gothenburg, June 2017

Contents

List of Figures	xi
1 Introduction	1
2 Theory	3
2.1 Electromagnetic theory	3
2.2 Digital holographic microscopy	4
2.2.1 Data analysis	4
2.3 Optical trapping	7
2.3.1 Calibration and calculating forces	8
2.4 Biological material	9
2.4.1 Using lasers on biological samples	10
2.4.2 Giant unilamellar vesicles	10
3 Method	13
3.1 Digital holographic microscope	13
3.1.1 Experimental setup	14
3.1.2 Data analysis	14
3.2 Optical trapping microscope	16
3.2.1 LabVIEW program	16
3.2.2 Calibration	18
3.2.3 Experimental setup	19
3.3 Cultivating cells and vesicles	19
4 Results and discussion	23
4.1 Yeast cells in digital holographic microscope	23
4.1.1 Discussion	25
4.2 Yeast cells in optical trapping microscope	26
4.2.1 Discussion	27
4.3 Model cells in optical trapping microscope	29
4.3.1 Discussion	32
5 Conclusion	35
Bibliography	37

List of Figures

2.1	The interference pattern seen in (a) is continuously recorded by the camera, with its Fourier transform seen in (b) . The leftmost peak is moved into the center of the coordinate system as in (c) . An inverse Fourier transform will then result in the final image seen in figure 2.2. Note that the image in (a) is best resolved in digital forms of this thesis, but not much can be seen in any format.	5
2.2	The image of several cell colonies in the DHM, inverse Fourier transformed from the image in figure 2.1c. The difference in brightness corresponds to phase difference created by the cells.	6
2.3	(a) A latitudinal displacement, where the beam gradient will push the particle to the left and the scattering force pushes upwards. (b) When the particle is in the center, there is no gradient force. (c) A particle below the waist will have both gradient and scattering force pushing it towards the waist. (d) The refractive and gradient force cancelling each other, leaving the particle slightly above the waist. (e) A higher numerical aperture will cause larger gradient force with a longitudinal displacement, meaning that the particle will rest closer to the waist compared to (d)	8
3.1	In both cases, the cells were bonded to the glass using Concanavalin A. (a) Setup using micropipette. (b) Setup using glass chip.	13
3.2	(a) Photograph of the experimental setup, where the glass chip can be seen connected to 15 mL vials, which in turn are connected to the pump by the blue tube. (b) The beamsplitter to the left controls at what angle the two beams are interfering, while the camera to the right records the interference pattern. (c) Systematic sketch of the DHM, where the sample is placed in a glass dish or a glass chip. . . .	15
3.3	User interface for the program controlling the translation stage. Controls are placed to the left and detectors to the right.	16
3.4	Block diagram of the LabVIEW program used. The four larger case frames in the center controls the automated movement.	17

3.5	(a) Photograph of the experimental setup. A USB cable is connecting the control tower to the left with a computer running the LabVIEW script controlling the translation stage. (b) Photograph of the top of the translation stage, the objectives and the sample holder. The sample is placed on a glass coverslip, firmly held in place by two clips. (c) Systematic sketch of the experimental setup.	20
4.1	(a) Yeast cells as seen in the DHM. A larger brightness contrast corresponds to a higher phase difference. (b) A 3D visualization of the cell colony where the topology corresponds to phase differences, not height of the sample. (c) The phase difference between light passing through the cells and the medium. The fluid exchange at 18 seconds can clearly be seen from the drop in phase differences.	24
4.2	The image of the cells as seen in the OTM, with a single cell captured. The scalebar is 10 μm	27
4.3	(a) By scanning over a fixed cell and registering the voltage response of the detector this correlation is detected. In a close distance to the center of the cell, the relation between voltage response and position is approximated by a linear fit. (b) The sensitivity ρ is calculated from the slope of the linear fit. (c) The deviation of the cell from the trap center as a function of time when using the Stokes drag calibration method.	28
4.4	Image of the MLV, GUV and bead. Since the GUV only consists of a single or a few lipid bilayers, it is not possible to resolve in this optical microscope. The scalebars are 10 μm . (a) The non-trapped bead stuck on the side of the GUV (b) The bead is pulled 14 μm , creating a membrane tube between bead and GUV.	29
4.5	(a) Voltage response to scanning over a fixed 2 μm bead. (b) The sensitivity ρ is calculated from the slope of the linear fit. (c) The deviation of the bead from the trap center as a function of time when using the Stokes drag calibration method.	30
4.6	Force profile from creating 14 μm tethers in the model cell. The red bar indicates for how long the bead was in movement, (a) Pulling for 3.3 seconds, using an average of 6 measurements. (b) Pulling for 3.3 seconds, using an average of 9 measurements. (c) Pulling for 6.8 seconds, using an average of 5 measurements. (d) Pulling for 22.5 seconds, using an average of 4 measurements.	31

1

Introduction

Since the first discovery of the cell by Robert Hooke in 1665, the study of cells have been a continuously evolving field. The optical microscope have been a good tool for studying the cell without interfering in its life cycle, giving information about its reproduction, growth and death. The optical microscope can even see into the cell, although its resolution is limited by the Rayleigh criterion $x = 1.22\lambda/\text{NA}$, where x is the minimum resolvable distance, λ the wavelength of light, and NA is the numerical aperture [23]. For a high NA, $x \approx \lambda \geq 400$ nm for visible light. Several methods have since been developed to significantly reduce the minimal resolvable distance [34].

Several methods have also been developed to gain information of the internal conditions of the cell. A. Ashkin and J. M. Dziedzic published in 1989 an article about optical trapping of a single living cells using an infrared laser [2]. Using the momentum of light and a tightly focused laser beam, a particle, a cell, or even a part of a cell, could be held suspended in i medium. The cell could in that way be totally controlled and manipulated without the observer affecting the cell itself. If a force were to affect the trapped particle, one could also calculate that force by finding the particle position relative to the trap. In 2005, an article about digital holographic microscopy, DHM, was published [18], based on previous work by F. Zernike [35, 36]. This was a non-invasive method of visualizing the composition of the living cell with sub-wavelength resolution. By using the coherence of a laser beam, the geometry of the sample cell will be reflected in a structured dephasing, which can be read out from an interference pattern.

This thesis describes a way of using a digital holographic microscope and an optical trapping microscope to enable the determination of the geometry, refractive index and cytosolic composition of a cell in a non-invasive manner. In the DHM, yeast cells will be exposed to solutions of changing refractive index by balancing sugars and salt concentration, while the OTM shows how information of the internal composition of the cell can be extracted from tether formation. Data from giant unilamellar vesicles, GUVs, will be used since they model the cell membrane without the adhesive force from the cytoskeleton. The cellular membrane is the largest organelle and responsible for several important processes of the cell, such as for example cell division, endocytosis and exocytosis [8].

The mapping of the cells in the DHM has a very high axial accuracy, below 20 nm, and the fact that the cells can be readily manipulated with an optical trap shows

great possibilities of further experiments combining these techniques with other microscopy techniques. By using an optical trap to pull membrane tubes, one also gains information about the lipid environment of the model cell.

Using label-free methods is a way to ensure studying cells in their native state, without the investigation or labelling affecting the native cell behaviour. Studies have shown that labelling with fluorescence might affect the cell behaviour [30, 16], while phototoxicity poses another threat [15].

Important cell properties like mass, volume, refractive index or age may be probed using label-free interrogation, and the transportation of cellular materials inside and between cells can also be mapped. Studying the generation and aging of the yeast cell, as a simple model in cell biology, have usage in a lot of separate disciplines; biomedical research, genetics and medicine for example [7, 26, 6]. Without fluorescence, label-free probing is often partially limited to optical resolution, although some approaches of fluorescence-free super-resolution has been investigated [1].

To draw bigger conclusions from the experiments performed, more data would need to be collected and the same experiment would have to be performed several times to increase the statistical significance. Control experiments have not been performed to verify the experimental setups, but comparisons to previous experiments are included.

This thesis covers the basic principles and theory needed to understand the methods used and results achieved in chapter 2, followed by a detailed explanation of the method and schematic sketches and description of the experimental setup in chapter 3. In chapter 4, the results are shown and discussed, while the final chapter 5, concludes the thesis and reflects on possible further studies.

2

Theory

To understand how the microscopes can probe the inside of biological material without contact, knowledge of optics are necessary. A brief introduction to electromagnetic theory is presented, but for a more thorough description, see source literature [12].

Section 2.2 describes how a light beam through the sample is affected by it, and how the information of the sample can be reconstructed. Section 2.3 describes how an optical trap works, with two different explanations for the two different trapping regimes. The determination of the trapping force using the Stokes drag calibration method is explained in subsection 2.3.1. Section 2.4 covers the biological aspects of this project and how the interaction between biological material and microscopes will affect the experiments performed.

2.1 Electromagnetic theory

Electromagnetic theory has been studied since 19th century, when visible light for the first time found its place in the electromagnetic spectrum. Ray optics, that was previously used, had to step aside for the more accurate description of wave theory. In the early 20th century, Einstein revealed another form of light quantized as a particle, the photon. This resulted in the wave-particle duality of light; two contradictory pictures that both explained different phenomena. De Broglie later showed that this duality concerned matter as well.

In a very thin band of wavelengths between 400 nm and 700 nm, electromagnetic waves have just the right energies to be registered in human eyes as visible light. Photons of higher energies, ultraviolet light, carries enough energy to break covalent bonds, while infrared light could cause molecular vibrations at most.

One of the most important physical constants is the speed of light in vacuum, c_0 . It can be formulated as a function of the vacuum permeability μ_0 and the vacuum permittivity ε_0 as

$$c_0 = \frac{1}{\sqrt{\varepsilon_0 \mu_0}}. \quad (2.1)$$

In a material, permittivity is a measurement of the materials ability to resist an electric field, often denoted with the relative permittivity $\varepsilon_r = \varepsilon/\varepsilon_0$. The refractive

index, n , is related to the relative permittivity and relative permeability as $n = \sqrt{\epsilon_r \mu_r}$, which means that the speed of light will be affected by the refractive index of a material as

$$c = \frac{c_0}{n}. \quad (2.2)$$

The refractive index also controls the angle refraction when light enters the medium at an angle according to Snell's law

$$n_1 \sin \theta_1 = n_2 \sin \theta_2. \quad (2.3)$$

Photons carries momentum, even though they are massless, with

$$p = \frac{E}{c} = \frac{h}{\lambda}, \quad (2.4)$$

where p is the particle momentum, E is the particle energy, h is the Planck constant, and λ is the wavelength. This means that it can exert forces on ordinary matter by exchanging momentum.

2.2 Digital holographic microscopy

Digital holographic microscopy, DHM, is a noninvasive microscopy method that can give information about geometry, optical properties and chemical properties of an object.

Since the speed of light in a material is inversely proportional to the refractive index, a beam of light propagating through a transparent object will carry information about the object, when compared to an undisturbed beam. A DHM is based on recording the interference pattern of two coherent laser beam, where one beam has propagated through a transparent sample. Recording the interference pattern with a camera enables a computer to recreate the sample from the interference pattern together with knowledge of the setup.

A difference between DHM and other microscopy techniques is that it is the hologram, the interference pattern, that is recorded, not the image itself. To get the image, one has to digitally reconstruct it using Fourier analysis. A Fourier transform of the interference pattern, see figure 2.1a, results in an image of the Fourier plane, figure 2.1b. Everything but the area marked with a rectangle is cropped out, resulting in the image in figure 2.1c, and an inverse Fourier transform produces the final result that can be seen in figure 2.2.

2.2.1 Data analysis

To extract the phase information from the sample, the refractive index and cell topology needs to be related to the measured phase difference, with the derived

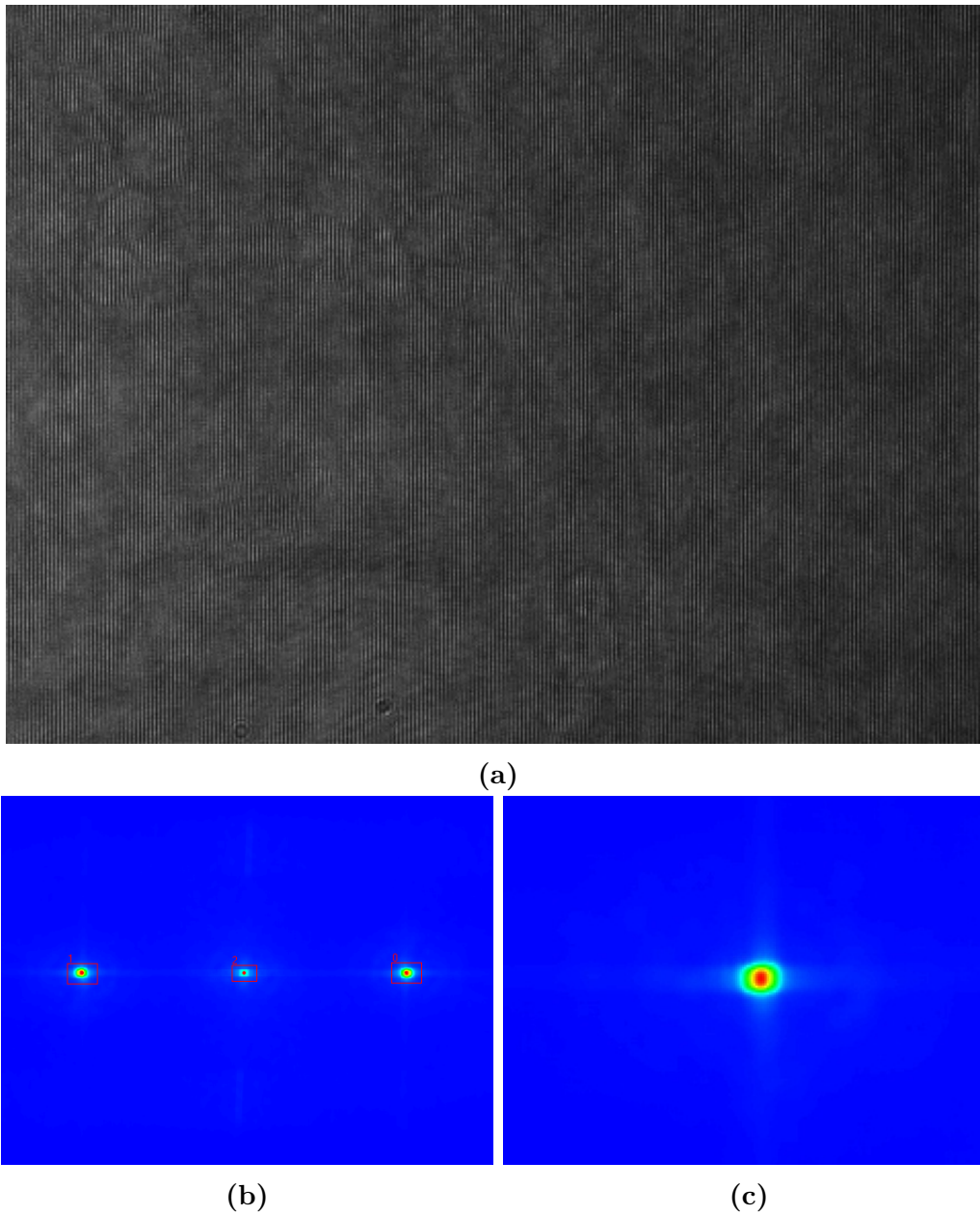


Figure 2.1: *The interference pattern seen in (a) is continuously recorded by the camera, with its Fourier transform seen in (b). The leftmost peak is moved into the center of the coordinate system as in (c). An inverse Fourier transform will then result in the final image seen in figure 2.2. Note that the image in (a) is best resolved in digital forms of this thesis, but not much can be seen in any format.*

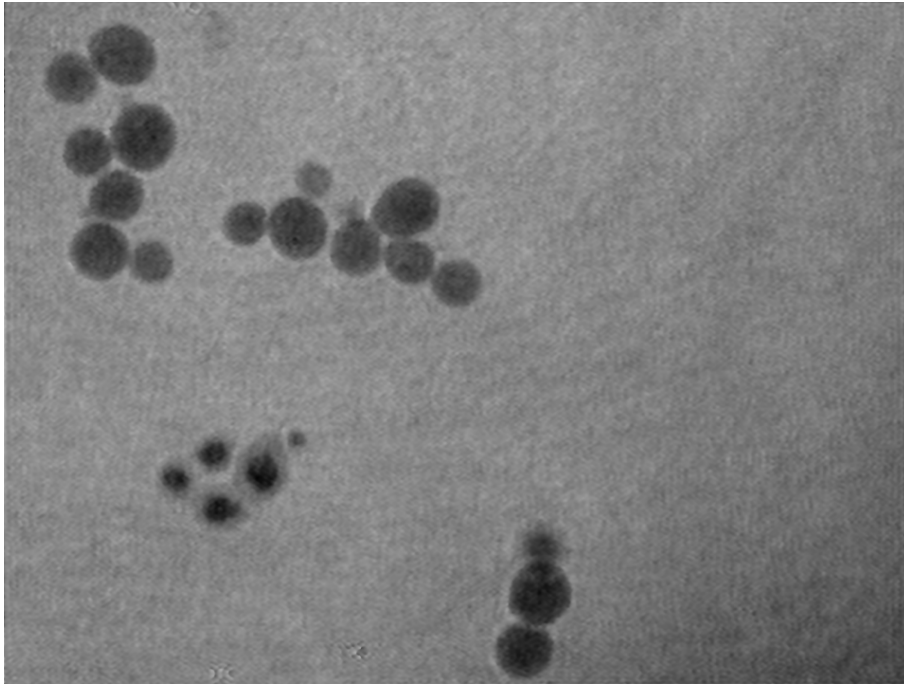


Figure 2.2: *The image of several cell colonies in the DHM, inverse Fourier transformed from the image in figure 2.1c. The difference in brightness corresponds to phase difference created by the cells.*

relation noted in equations (2.7) and (2.8).

The Helmholtz equation with inhomogeneous dispersion is denoted as [20]:

$$\nabla^2 \Psi(\mathbf{x}) + k^2 n(\mathbf{x})^2 \Psi(\mathbf{x}) = 0 \quad (2.5)$$

with $\Psi(\mathbf{x})$ being the optical field, $k = 2\pi/\lambda$ the wavenumber and $n(\mathbf{x})$ the local refractive index. When considering the refractive index and topology of the cell as slowly varying functions, the WKB approximation could be used on equation (2.5):

$$\Delta\varphi \approx kz(n_0 - n_{cell}), \quad (2.6)$$

where z is the cell topology or cell height, n_0 is the refractive index of the solution surrounding the cell, n_{cell} is the refractive index of the cell. If n_{cell} is known, the topology of the cell can be calculated. If n_{cell} is unknown, it can be calculated by making a second measurement on the same cell in a different medium. This second medium needs to be a solution with equal osmotic pressure but different refractive index than the first buffer solution. So by measuring the phase difference between cells and background for two different solutions, both cell topology z and refractive index n_{cell} can be extracted as:

$$\begin{cases} \Delta\varphi_0 \approx kz(n_{cell} - n_0) \\ \Delta\varphi_{sol} \approx kz(n_{cell} - n_{sol}) \end{cases} \Rightarrow n_{cell} \approx \frac{\Delta\varphi_0 n_{sol} - \Delta\varphi_{sol} n_0}{\Delta\varphi_0 - \Delta\varphi_{sol}}, \quad (2.7)$$

$$kz \approx \frac{\Delta\varphi_0 - \Delta\varphi_{sol}}{n_{sol} - n_0}, \quad (2.8)$$

where n_{sol} is the refractive index of the second solution and φ_{sol} is the measured phase difference when using the second solution. This equation calculates z as the average height over the whole cell, and the maximum cell height will be $3z/2$.

2.3 Optical trapping

Optical trapping is a way of controlling and positioning particles in three dimensions by letting the momentum of light transfer into a trapped particle. This section describes what parameters affect the trapping strength and how it is calibrated.

Consider a dielectric particle in a tightly focused Gaussian laser beam. With a non-absorbing particle, the light will refract on the interfaces between the surrounding medium and the particle and change direction, as according to Snell's law, equation (2.3). If the particle is not positioned in the beam waist, where the intensity is the highest, the light will change direction as can be seen in figures 2.3a and 2.3c, where a thinner line represents a smaller light intensity or less photons. Since the light and its momentum vector changes direction, and the total momentum of the particle and light must be conserved, the particle gains an antiparallel momentum. The particle will therefore be pushed by gradient forces towards the waist of the beam, both in lateral and longitudinal direction [2]. Exactly how it is pushed will vary with the exact size and shape of the particle, why a predictable result is only given from spheres or ellipsoids [37].

There will also be a scattering force, which inherently pushes the particle along the light direction. When the particle is in the beam waist, the net momentum change of the light pushes the particle upwards. The particle will therefore find its equilibrium position when gradient and refractive forces are equal, as in figure 2.3d, which is slightly above the waist. This is commonly countered by using a high numerical aperture, as seen in figure 2.3e. That means that the longitudinal energy will not be as large as with lower numerical aperture, figure 2.3d. The displacement necessary for the gradient force to equal the refractive force will be much smaller, so the equilibrium position will be closer to the waist.

This explanation, based on ray optics, holds for the Mie regime, where the particle radius $r \gg \lambda$. If $r \ll \lambda$, the Rayleigh regime, ray optics is no longer valid. The particle can then be considered as a dipole in an electromagnetic field. To minimize its own energy, the particle will be attracted towards the highest energy area, where the electromagnetic field has the highest intensity, i.e. in the waist. The trapped particle is still subjected to scattering forces, why the particle will find equilibrium slightly off the waist, the same as in figures 2.3d and 2.3e. In the Rayleigh regime, the force is not as dependant of particle shape, since it is the energy minimization that pulls the particle towards the waist, not geometry [3].

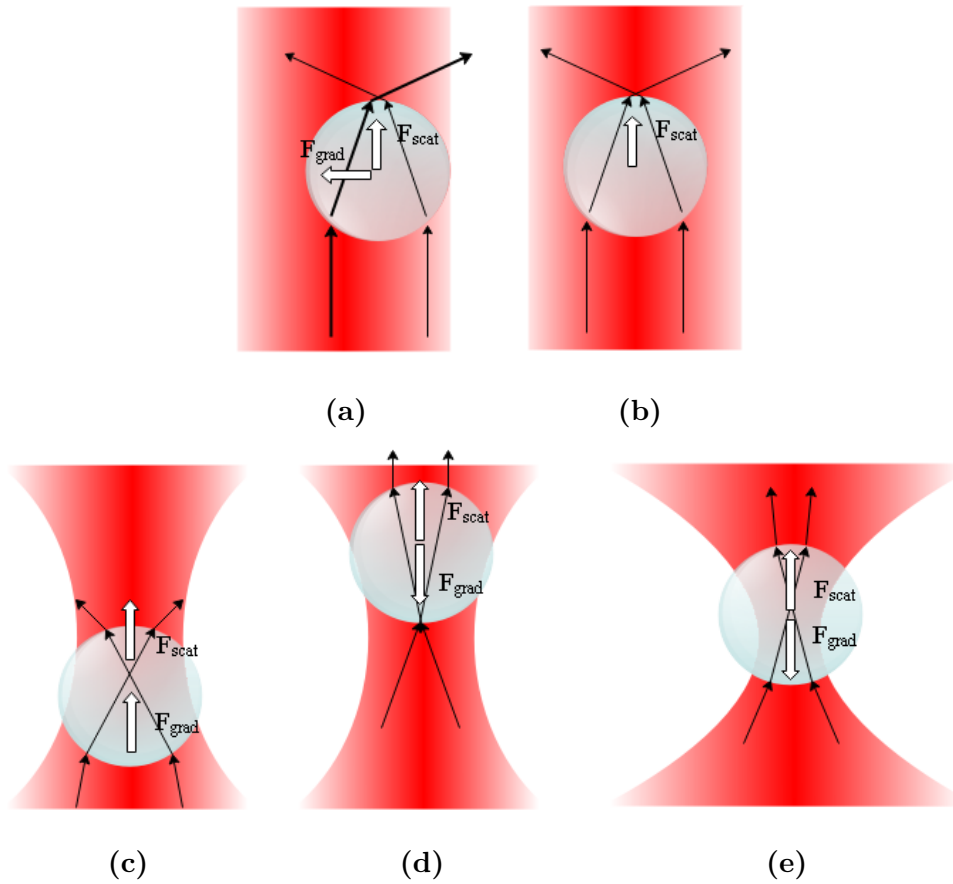


Figure 2.3: (a) A latitudinal displacement, where the beam gradient will push the particle to the left and the scattering force pushes upwards. (b) When the particle is in the center, there is no gradient force. (c) A particle below the waist will have both gradient and scattering force pushing it towards the waist. (d) The refractive and gradient force cancelling each other, leaving the particle slightly above the waist. (e) A higher numerical aperture will cause larger gradient force with a longitudinal displacement, meaning that the particle will rest closer to the waist compared to (d).

The most relevant regime for experiments is often between Mie and Rayleigh, $0.1\lambda < r < 10\lambda$, the so-called meso regime. The theoretical framework around this regime is not as clearly mapped as the others, but there are simulation toolboxes developed for modeling how the optical trap works together with different shapes and sizes [21].

2.3.1 Calibration and calculating forces

To convert voltage data from the quad detector to data on the forces affecting the bead, both the linear relation between detector voltage and displacement and the linear relation between displacement and force needs to be established.

When the particle is close to the beam waist, closer than half the particle radius within the focal region, the force on the particle from the trap can be modelled as

a spring force:

$$F_{trap} = -kx, \quad (2.9)$$

where k is the trap stiffness and x is the distance between the particle center and laser beam center [37]. To calculate the trap stiffness, subjecting the trapped particle to a known force enables finding the proportionality to the particle deviation.

For a spherical particle moving in a medium, the Stokes drag force F on a spherical particle can be expressed as [37]:

$$F_{drag} = 6\pi\eta rv, \quad (2.10)$$

where η is the medium viscosity, r the particle radius and v the velocity of the particle relative to the medium. If the particle is moving at a constant velocity relative to the medium, it may reach a stationary state, where the drag force and the trap force are equal. By finding the distance x for a specific v , k could be calculated as:

$$F_{trap} = F_{drag} \Rightarrow -kx = 6\pi\eta rv \Rightarrow k = \frac{6\pi\eta rv}{-x}. \quad (2.11)$$

This is the Stokes drag calibration method and it is a common way of calibrating, but requires precise distance determination and accurate and reproducible movement of the translation stage holding the sample. It requires a constant velocity, and measurements can not include acceleration or turning. To find the maximum force applicable to a particle in the trap, one can see at what velocity the drag force exceeds the trapping force. By increasing the relative velocity of the particle and find the velocity where the particle leaves the trap, $F_{trap} < F_{drag} = 6\pi\eta rv$. The minus sign in equation (4.2) originates in v and x being in opposite directions, and should be neglected if absolute values are used.

When the stiffness of the trap is determined, the forces on the particle can be calculated by the spring force equation. By registering the position of the particle relative to the trap, the forces acting on the particle can be calculated. To efficiently determine the position of the particle relative to the trap, a quad detector can be used. Since the laser beam will refract because of the trapped particle, the deflection can be used to determine the particle position. A particle off-center will therefore change the angle of the beam as a function of its position, and this angular change can be precisely registered by the quad detector. By scanning over a fixed particle while simultaneously collecting data from the detector, the detector response to a known particle displacement can be mapped.

2.4 Biological material

Even though *Saccharomyces cerevisiae*, the yeast cell, are one of the most robust and vigorous cell types, there are some things one need to pay extra attention to. Since a laser beam used in an optical trapping microscope will be focused as tightly as possible, extra precautions has been paid to laser wavelength, laser power and temperature. Theory connecting the model cell to a real cell membrane are also

presented.

2.4.1 Using lasers on biological samples

One problem that occurs when studying biological samples with lasers is the absorption of light in the sample. This could cause damage to the material, or heating of the sample or its environment. A wavelength with minimal impact would be one with low energy and minimal absorption. Every organic material have a different absorption spectra, but shorter wavelengths are more commonly absorbed and carries more energy. Wavelengths above 800 nm has significantly lower absorption and lower energy, causing considerably less damage on biological samples [37]. Since a shorter wavelength decreases the size of the focus, and therefore increases the trapping power for smaller objects, wavelengths between 790 and 1064 nm are commonly used [37].

Another factor is the intensity used. For DHM, the quality of the image is basically indifferent to intensity, which means that any intensity low enough to not damage the sample can be used. The beam is not focused either, which allows for significantly higher laser powers. For optical trapping, having a higher intensity means bigger control of the trapped particle. The beam will also be focused with a lense, making the matter more sensitive than for DHM. Using a high numerical aperture will also increase the trapping strength, which allows reducing the laser power needed and minimizing potential damage.

Since energy from the trapping light may be absorbed by the medium, this may affect the temperature of the medium. For water, this effect is approximately $8 \text{ K W}^{-1} = 8 \text{ mK mW}^{-1}$ [24]. For powers in the milliwatt range, this effect can therefore be disregarded for experiments where the temperature is not of extraordinary importance.

2.4.2 Giant unilamellar vesicles

Giant unilamellar vesicles, GUVs, consists of a single lipid bilayer. They are conventionally accepted as a simple model that can approximate the behaviour of the cellular membrane [8].

The membrane tension T of a cell is affected by the lipid surface tension T_m and a term γ representing the membrane-cytoskeleton adhesion as [13]:

$$T = T_m + \gamma = \frac{F_0^2}{8B\pi^2}, \quad (2.12)$$

where F_0 is the static tether force from the cell surface and B is the bending stiffness of the membrane. Since the GUVs do not have a cytoskeleton, only T_m will contribute, and by using F_{GUV} as the static tether force for the model of a cell without

cytoskeleton, the tension can be denoted

$$T_m = \frac{F_{GUV}^2}{8B\pi^2}. \quad (2.13)$$

By comparing the difference in the static tether forces, the submission from the membrane-cytoskeletal adhesion, F_{ad} , could be calculated as $F_{ad} = F_0 - F_{GUV}$. B can be assumed a constant representing a typical value for lipid bilayers, $B = 2.7 \times 10^{-19} \text{ N m}$ [10].

A GUV can be used as a first approximation of a cell membrane [33]. Without its cytoskeleton, it is generally fluidic enough to allow manipulation and can therefore be used for pulling membrane tethers.

3

Method

Both microscopes are built in-house; designed and improved as the project went along. The optical trapping microscope was built from scratch during this project, which demanded creating a layout of the microscope for the components available, adjusting the microscope after the experiments to be performed and buying optical components that were needed; see details in section 3.2. The digital holographic microscope was already assembled, but two methods of creating an efficient fluid exchange were evaluated; the two different variants are described in section 3.1.

Sketches of the experimental setups can be seen in figures 3.2c and 3.5c. Every detail is not included, but the basic components can be seen. There are also several photographs of the microscopes. Procedures and protocols for handling the microscopes and cell cultivation are noted, so that they may be reproduced. The basis for the protocol for producing GUVs are based on the commonly used protocol at the Biophysical laboratory at Chalmers University.

3.1 Digital holographic microscope

The holographic phase microscope uses a 633 nm laser together with two beamsplitters, several lenses and polarizers and a CCD camera. The camera is connected to a computer where a LabVIEW program collects and transforms the data.

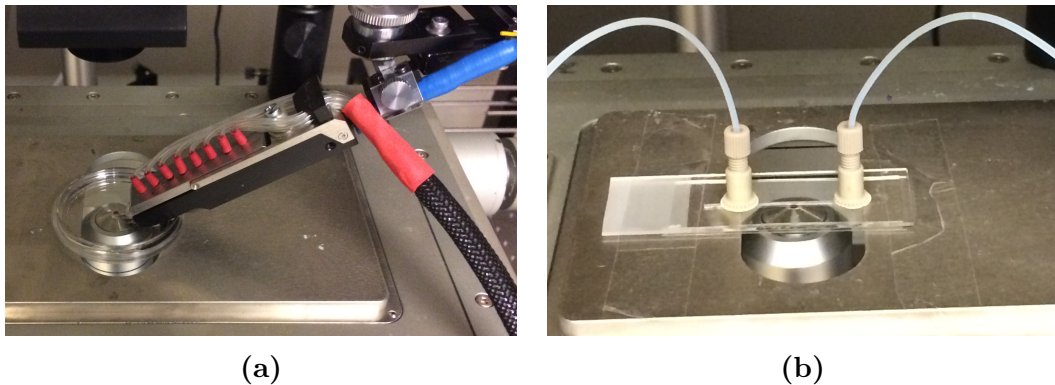


Figure 3.1: *In both cases, the cells were bonded to the glass using Concanavalin A. (a) Setup using micropipette. (b) Setup using glass chip.*

A limiting factor of this setup when using the system in real time is the computational analysis. Since there are several transforms to every frame, the maximum recording frame rate is around 5 fps. When instead doing the transformations in post production, the maximum recording frame rate is at least 50 fps. The resolution of the final images and data is limited by the resolution of the camera, imperfections in optical parts and disturbances in the interference pattern from reflections in the objective.

Initially an EpiPen, a microfluidic pipette from Fluicell seen in figure 3.1a, was used to replace the environment of the sample cells with different solutions. Later, a glass chip was built with a single channel and a well at each side. The channel, approximately $1.5 \times 0.75 \text{ mm}^2$, can hold approximately 50 μL , and it can be seen in figure 3.1b. To exchange the fluid inside the channel, a pressure is applied to a vial connected to the chip, which forces the fluid into the chip. A complete exchange of the medium in the chip takes less than 1 second.

To verify that the setup enabled a quick and complete fluid exchange, trypan blue were used to enable a simple visual verification. A fluid pulse length of 8 seconds at 150 mbar were deemed sufficient. The refractive indices of mediums used were measured using a refractometer.

3.1.1 Experimental setup

The experimental setup can be seen in figure 3.2c. The Gaussian beam from a Uniphase laser with $P = 35 \text{ mW}$, $\lambda = 633 \text{ nm} \Rightarrow k = 9.93 \mu\text{m}^{-1}$, is polarized and expanded. A beamsplitter divides the beam depending on polarity; the light distribution is controlled by the angle of the first polarizer. One beam is going through the sample and a $40\times$ Leica objective, while the other beam is undistorted. For the interference pattern to appear, the polarization of the two beams needs to be aligned, why a $\lambda/2$ plate is used on the undistorted beam. Another beamsplitter couples the two beams at an angle controlled by the mirror, which creates an interference pattern recorded by an Allied Vision Prosilica GX1920 CCD camera at 4 fps.

If the micropipette is used, the sample is placed in a Petri dish, and the pipette is placed in a manual coarse manipulator. With the glass chip, the cells are placed in the chip by pumping; both setups uses a Fluicell pump.

3.1.2 Data analysis

The camera images are saved in LabVIEW as .avi-files. A Matlab script transforms the images as described in section 2.2. At this stage, crossection area and distances can be measured by knowing the pixel size. The images are then analyzed with ImageJ, to identify the cells and separate them from the background. This information is imported into Matlab, where the average light intensity over each cell is calculated and compared to the average background intensity. As described in section 2.2.1,

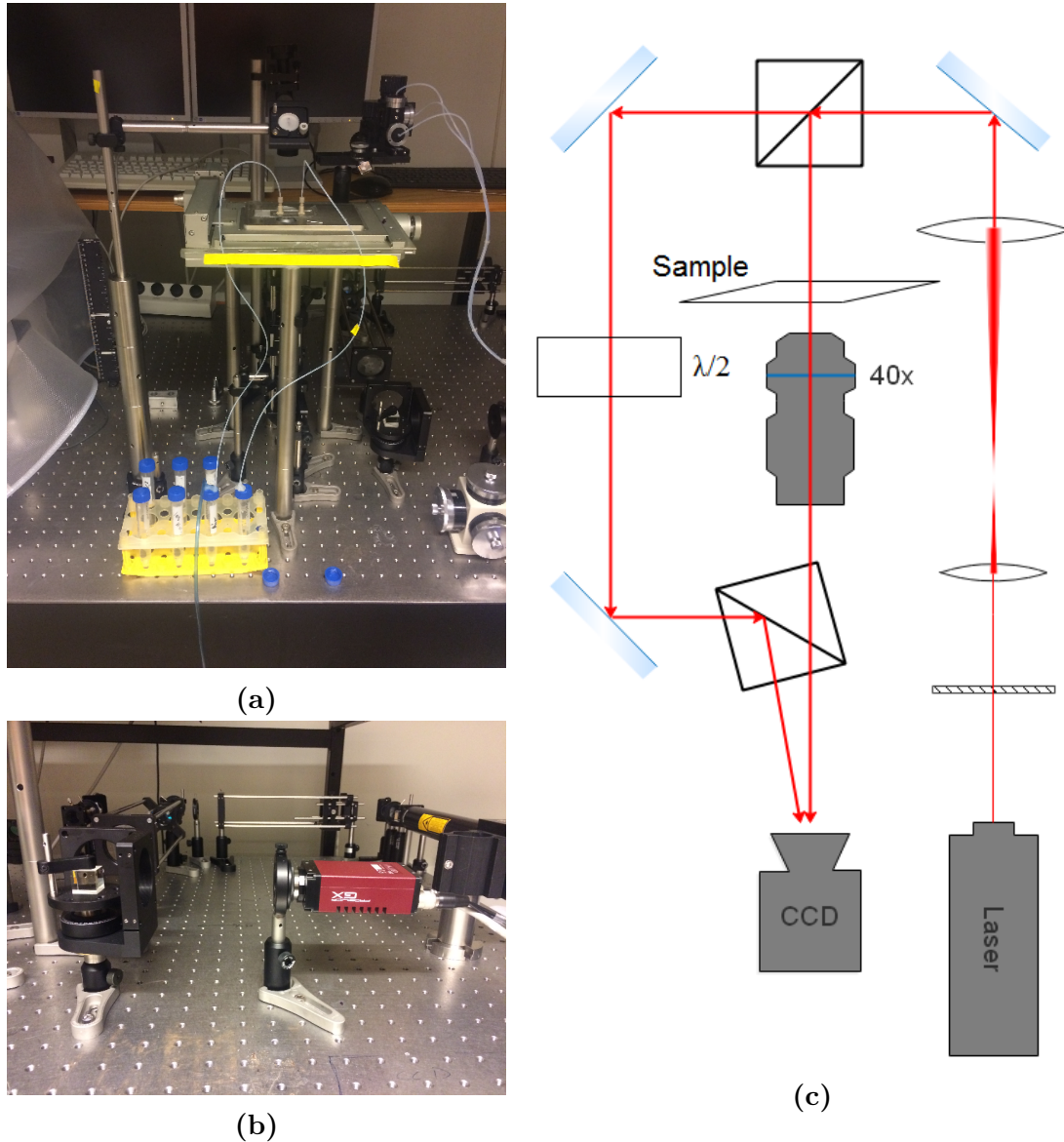


Figure 3.2: (a) Photograph of the experimental setup, where the glass chip can be seen connected to 15 mL vials, which in turn are connected to the pump by the blue tube. (b) The beamsplitter to the left controls at what angle the two beams are interfering, while the camera to the right records the interference pattern. (c) Systematic sketch of the DHM, where the sample is placed in a glass dish or a glass chip.

3. Method

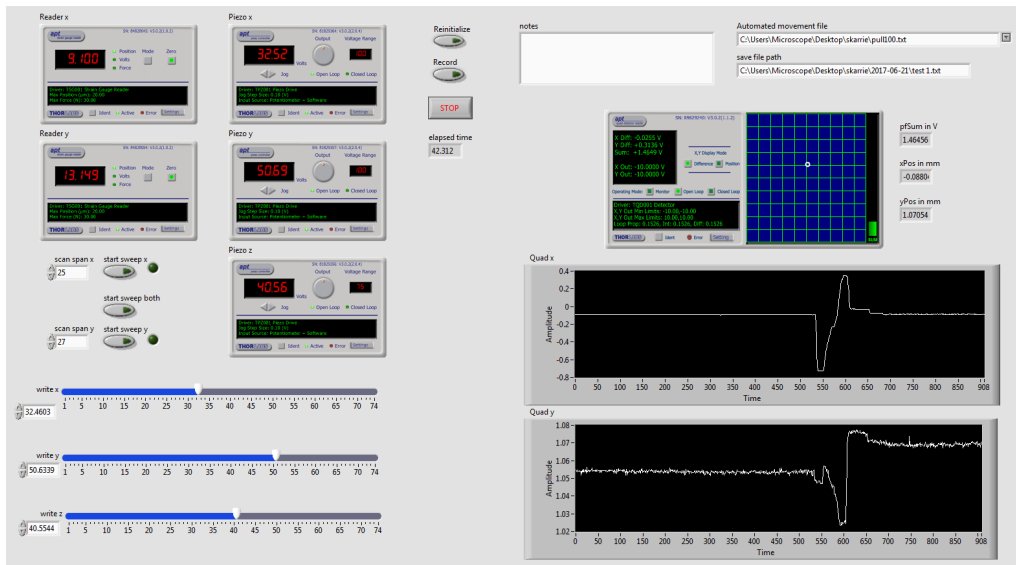


Figure 3.3: User interface for the program controlling the translation stage. Controls are placed to the left and detectors to the right.

the intensity of the light is directly related to the phase difference, so the phase difference for each cell can then be calculated.

3.2 Optical trapping microscope

The optical trapping microscope is based on the modular optical tweezers system with a force acquisition module from Thorlabs [31, 32]. Two variants of the lens setup were used; one where the beam expander and divergence control were separated, and one where they were combined. The disadvantage with the combined system is that the size of the beam is inherently coupled with the divergence, but it reduces the experimental complexity. Ultimately, both system works fine, and the latter were mainly used.

A 40 \times objective were chosen as the magnification were sufficient for this setup. Different condenser lenses were considered but the 10 \times ultimately was easy to incorporate into the setup and proved sufficient.

For tracking the laser beam, a quad detector was used. The voltages from the quad detector was fed into LabVIEW, where the laser beam deflection was calculated.

3.2.1 LabVIEW program

The software was created in LabVIEW and enabled computer control of the translation of the sample on the 3-axis stage, up to 15 μm in each dimension. The interface of the program can be seen in figure 3.3, where the controls are placed on the left hand side of the screen, and detectors on the right hand side. The two larger graphs

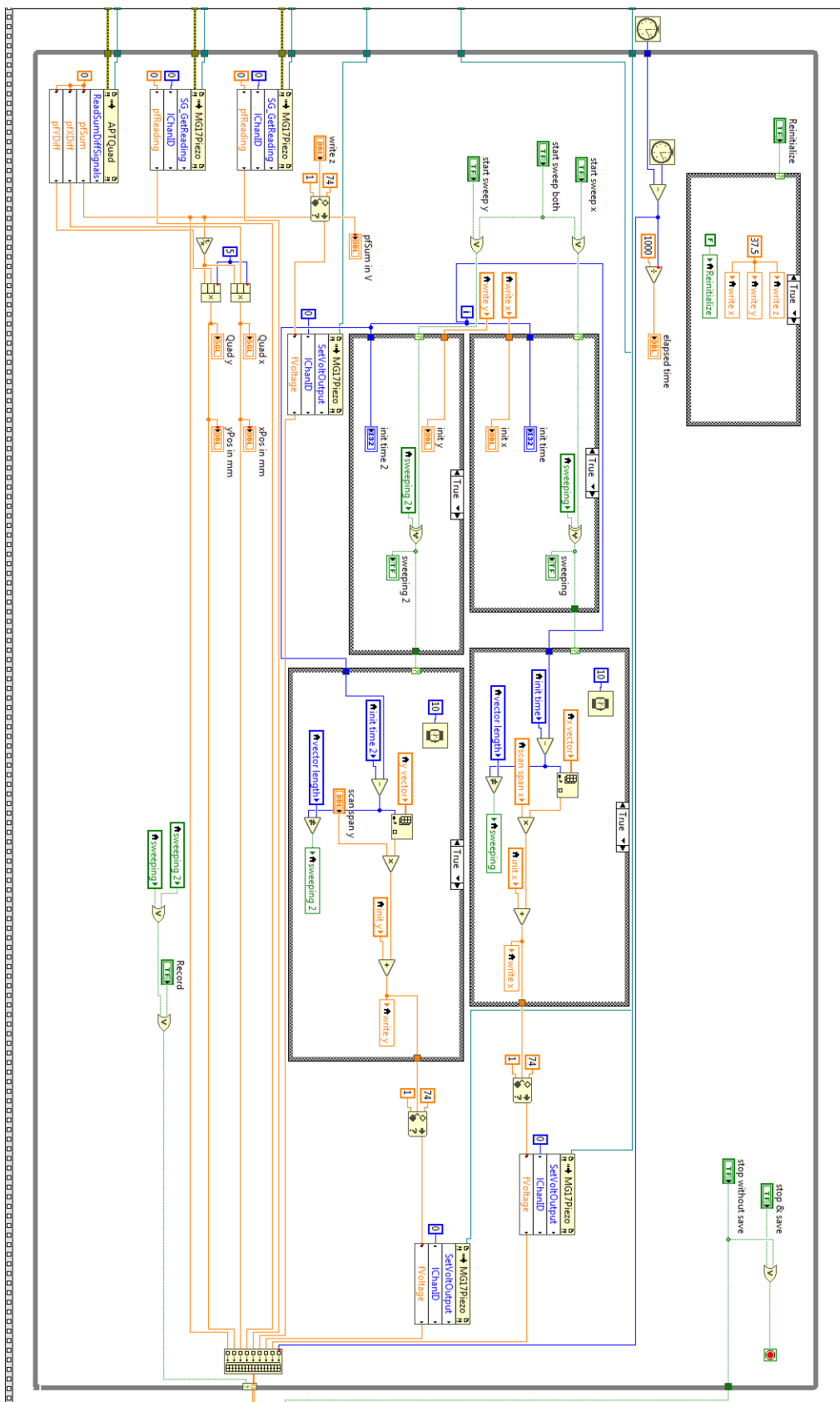


Figure 3.4: Block diagram of the LabVIEW program used. The four larger case frames in the center controls the automated movement.

shows the temporal development of the detector voltages during one minute, where the indices corresponds to data points collected.

The corresponding block diagram can be seen in figure 3.4, showing the major loop of the program. The input to the translation stage can be either a prewritten vector or matrix or manually moving the knobs seen on the front panel. The data is collected to the very right, where it is saved to a *.txt* file. Some features, like autofocus and automated synchronization between video and data were developed but not compatible with the final program.

Several different setups were used with two different cameras. Initially, the video recording using a Thorlabs CCD camera were done in the same LabVIEW VI as detector data were collected. This resulted in good control and easy synchronization of video and data, but significantly reduced flexibility. The setup did not allow collecting data from the detectors at a different rate than the video framerate, and the two processes slowed each other down. Another attempt were made at using the same camera with Thorlabs separate video recording software. This allowed different framerates, but it were not as flexible as when a LabVIEW program controlled the camera.

The best solution for both flexibility and speed were when the video recording were controlled and saved by a different computer, running a parallel LabVIEW program. With an Allied camera connected to the Ethernet outlet, combined with the possibility to crop the image, frame rates of 100 fps were possible, while the data collection via USB on the first computer ran at 24 data points per second.

3.2.2 Calibration

The calibration is done in two steps. First, the trap strength is to be determined. For every combination of particle, medium, and laser settings, the trapping strength will differ. It is important to calibrate for exactly the setup that is to be used. The Stokes drag calibration method was used to find the trap constant. The translation stage was moved, and the particle deviation was registered with the quad detector. Because of the limited range of the automated movement of the translation stage, the movement will be back and forth for 25 cycles, and the average displacement in full velocity will be used. The calibration was done at a distance of 10 μm , since a proximity to the glass surface could affect the calibration [9]. To calibrate the quad detector, a grid scan was performed over a fixed particle and the detector response was mapped against the known grid distances. Data analysis were done in Matlab, while ImageJ was used to extract distances and sizes.

The Stokes drag calibration method should optimally be used when particles can be dragged at a constant velocity for some time. Since a certain velocity was needed to get deviations significantly higher than the background noise, restrictions on the automated movement only allowed constant velocities for a very finite time period, less than 0.3s. This means that the particle had to be dragged back and forth with

rests in between, and only the particle deviation at the middle of the movement was used for calibration. This may be a source of error in the calibration of the trapping strength; other calibration methods were not used to verify the trapping strengths. An average of 50 data points were used.

3.2.3 Experimental setup

The experimental setup can be seen in figure 3.5c. A Thorlabs laser was used at $\lambda = 1064$ nm, mounted in a butterfly mount. The laser beam is expanded by the first two lenses, and two 50 mm lenses were used to control the divergence of the beam. To compensate for the scattering force, the beam came into the objective slightly converging, which made the trapped particle in the optical focus. An oil immersion 40x Olympus objective was used, together with a 10x Olympus objective used as a condenser. Two dichromatic mirrors were used to separate the visible light, represented by yellow arrows, from the infrared light, red arrows. The light source is a single emitter white light LED and the optical microscope image is recorded by an Allied Manta G-235 CCD camera.

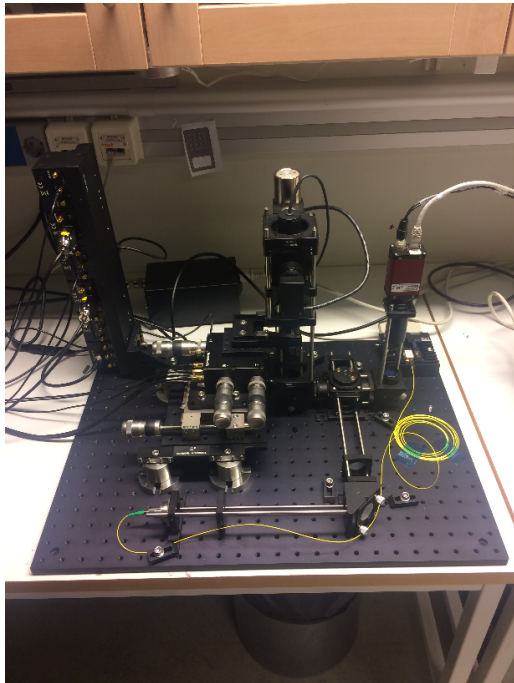
The automated movements were performed using a Thorlabs 3-Axis NanoMax Flexure Stage connected to a computer with LabVIEW by using Thorlabs T-cube piezo driver and T-cube strain gauge reader. The quad detector is a Thorlabs T-Cube PSD Auto Aligner, also connected to LabVIEW. The post-processing of data were done in Matlab.

3.3 Cultivating cells and vesicles

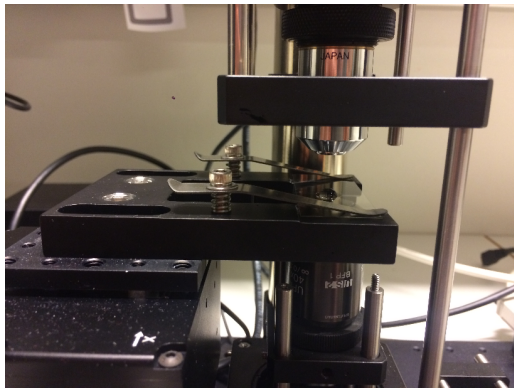
Saccharomyces cerevisiae were initially brought frozen from Sahlgrenska University Hospital and the yeast is cultivated in the lab by diluting a small sample from previous cultivation in a solution of glucose and nutrients. 1 mL of yeast cells were added to 10 mL of a nutrient solution and 1 mL glucose. To make the cells stick to glass surfaces during experiments, Concanavalin A was used. ConA is a common protein used for immobilizing the cell without limiting its ability to change size or bud [27].

The GUVs were grown out of 5 μ L lipids, treated in a vacuum desiccator for 18 minutes to reduce fluids, and then wetted with 350 μ L HEPES buffer. The production of GUVs from MLVs, multilamellar vesicles, are spontaneous, and with this process, there will be GUVs of different concentrations and sizes.

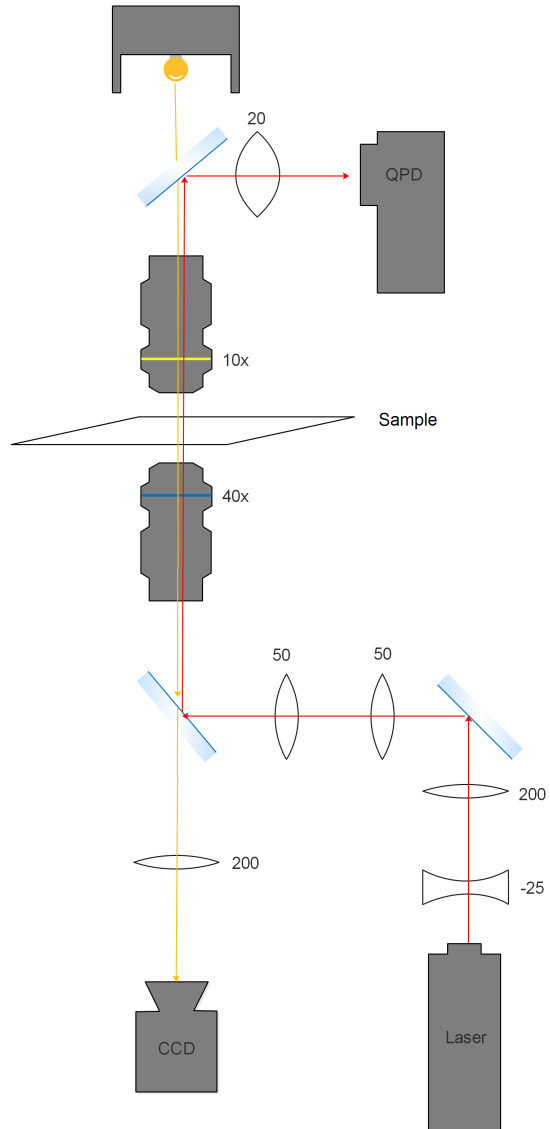
Several lipids with biotin in the range of 5 % to 20 % were investigated, but ultimately only lipids containing 5 % biotin was used. The lipids using more biotin were not as inclined to creating GUVs. The lipids were a blend of 48.4 % ATTO488-DOPE, 31.3 % SPE and 30.3 % DOPS. The ATTO488-DOPE was purchased from Atto-Tec, all other products from Avanti Polar Lipids.



(a)



(b)



(c)

Figure 3.5: (a) Photograph of the experimental setup. A USB cable is connecting the control tower to the left with a computer running the LabVIEW script controlling the translation stage. (b) Photograph of the top of the translation stage, the objectives and the sample holder. The sample is placed on a glass coverslip, firmly held in place by two clips. (c) Systematic sketch of the experimental setup.

Polystyrene beads with a diameter of 2.0 μm were mixed with the lipids after 6 minutes in the vacuum desiccator. The beads, ordered from Polysciences Europe, were coated with streptavidin. The streptavidin binds the bead to biotin in the lipids with an association constant of $K_a = 10^{15} \text{ mol}^{-1}$, which makes the bond fast and basically irreversible. The bond is also very strong, almost as a covalent bond [25]. The beads, originally with a 1.25 % particle concentration, were diluted 1:500 before 1.0 μL were added to the lipids.

4

Results and discussion

The results from the three main parts of this project is here presented. The discussion following each part will also examine and contextualize the result. The main results from analyzing the refractive index and volume of the cells can be found in figure 4.1c and table 4.1, while the results from tether formation of the GUVs can be seen in figure 4.6a-4.6d.

Attempts were also made at trapping beads smaller than $1\ \mu\text{m}$. Though the trap should optimally handle $1.0\ \mu\text{m}$ beads well, it did not result in a high enough trapping strength. For smaller beads, $0.5\ \mu\text{m}$ and $0.2\ \mu\text{m}$, the gradient forces could not match the refractive forces, and no consistent trapping were possible.

Note that the experiments here presented have not been verified using repeatedly performed experiment, but a platform were established to enable the interrogation of samples in a label free way and the results here presented shows proof of principle, validating the design and implementation strategy.

4.1 Yeast cells in digital holographic microscope

This first section describes experiments using the DHM. An evaluation of the two different sample holders is followed by the results from extracting refractive index and geometry of a cell colony.

The initial DHM setup was using the microfluidic pipette, seen in figure 3.1a. These experiments could not produce valid reproducible data, because of practical limitations of both the setup and material properties. Since the image is produced by interference of light, the background scattering needs to be minimal. The pipette would therefore need to be placed at a large distance, at least $100\ \mu\text{m}$, and that made it hard to position it with full control. Even though there were clear evidence of the cell being surrounded and affected by the medium flowing out from the pipette, there was no way of saying if the cell were completely surrounded by the new medium.

The construction of the glass chip significantly improved the setup. The millifluidic system made sure that the medium exchange was fast and that the new medium completely surrounded the cells. All results published from the DHM is using the glass chip, as no reliable data was extracted using the pipette.

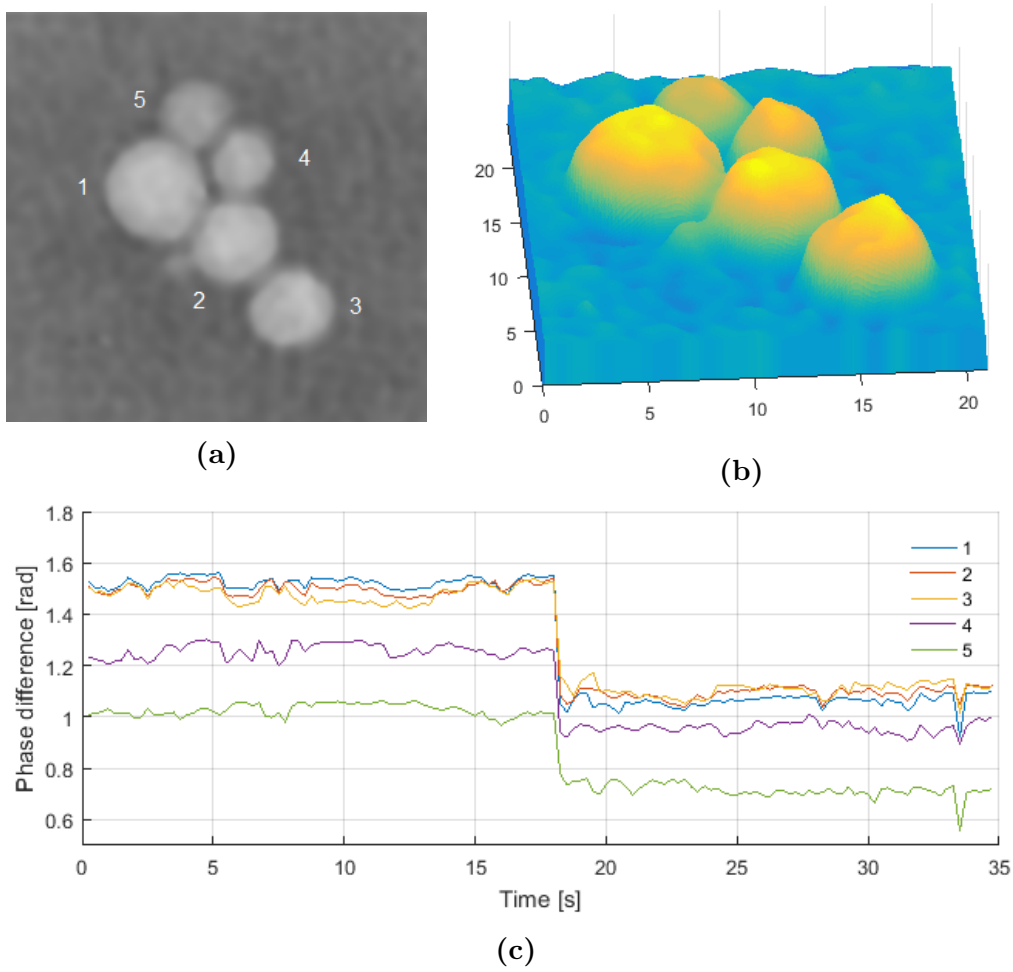


Figure 4.1: (a) Yeast cells as seen in the DHM. A larger brightness contrast corresponds to a higher phase difference. (b) A 3D visualization of the cell colony where the topology corresponds to phase differences, not height of the sample. (c) The phase difference between light passing through the cells and the medium. The fluid exchange at 18 seconds can clearly be seen from the drop in phase differences.

A colony of yeast cells, *Saccharomyces cerevisiae*, was studied in the DHM, see figure 4.1a. A 3-dimensional visualization can be seen in figure 4.1b, where the height corresponds to the light intensity in figure 4.1a. The interference pattern was recorded, and the phase differences were extracted as described in section 2.2. In figure 4.1c, the resulting change in phase difference can be seen when the medium around the cells are completely exchanged from phosphate citrate buffer with $n_0 = 1.337$ and a 0.45 mMol sucrose solution with $n_{sol} = 1.355$. The concentration of the sucrose solution used is to maintain the same osmolarity of the phosphate-citrate buffer, 0.45 mOsm, which means that the cells should not be affected by the fluid exchange in the short term.

By calculating an average of the phase difference $\Delta\phi_0 = 1.520$ in the phosphate-citrate buffer and $\Delta\phi_{sol} = 1.070$ in the sucrose solution for the biggest cell and using

Cell	$\Delta\phi_0 - \Delta\phi_{sol}$	Refr. index	Height / μm	Volume / μm^3
1	0.450	1.398	3.78	123.4
2	0.383	1.407	3.22	69.0
3	0.349	1.412	2.93	60.9
4	0.298	1.392	2.86	39.0
5	0.341	1.414	2.50	30.2

Table 4.1: Data from analyzing the phase differences in figure 4.1c and equations (2.7) and (2.8). The calculation of the volume is assuming a spherical or ellipsoid cell.

equation (2.7), the refractive index for the cell is calculated to $n_{cell} = 1.398$. The refractive indices for the other cells may be found in table 4.1

By using equation (2.8), the maximum height of the particles as numbered in figure 4.1a was calculated, with a maximum for cell 1 with $3.78 \mu\text{m}$. Assuming that the cell maintains an approximately ellipsoid shape, the volume V of the cell can be calculated as $V = 2Az/3$, where A is the cross section area and z is the cell height. By measuring the cross section cell area from the DHM images, the volume of the cells can be calculated, with the biggest cell measuring $123.4 \mu\text{m}^3$. The volume for the other cells ranged between $30 \mu\text{m}^3$ and $69 \mu\text{m}^3$, as can be seen in table 4.1.

4.1.1 Discussion

These cells are being observed in a living and growing period, which causes them to change over time. In the images, a small bud is clearly visible. That means that material from the connected cell will be transported into the bud, while the parent cell will produce new material, not necessarily at the same rate. This experiment only took 35 seconds, but a longer measurement would definitely be affected by this.

The small bud may also affect the computer analysis. Since a particle analysis routine in ImageJ is used for recognizing the individual cells, a small bud may be hard to identify. A filter is therefore used to disregard potential cells that are too small. The imaging programs will therefore recognize the small bud that can be seen in figure 4.1c as background, which slightly skews the final result, since the software compares the background intensity to the cell intensity.

After budding, the cells still have a covalent bond between them for a longer time, and will stay very close to each other. The cell identification software may therefore have a harder time separating the different particles, since they are all so close to each other. At 6 seconds in figure 4.1c, a decrease in phase difference can be seen for three cells, while two cells have an increase in phase difference. This may be explained by an error in identification of the cells in these frames, since no material should be exchanged by these cells, nor this fast. If just a few frames were used, every frame could be checked manually, but even for this short experiment at low

frame rate, 4 fps, the amount of work is not practicable.

The video footage shows a particle or air bubble quickly passing by next to the cells out of focus at 34 seconds in figure 4.1c. This leads to a smaller phase difference between the cells and the background, which causes the dip. Other sudden fluctuations is probably because of similar effects that is not visible on the footage. There is no flow of the fluids at this time, but there may still be remnants of previous fluid exchanges. This can also explain the slight turbulence right before and after the drop in phase difference at 18 seconds. During a couple of seconds, the new fluid will be pressured into the system, but the interface between the fluids have not yet passed the region of interest. The fluids will be flowing for a couple of seconds before and after the fluid interface has passed the region of interest. Even though the cells should be anchored to the glass with ConA, some biological material may still be released.

When trying to compare these results to literature, no data for the refractive index of single yeast cells were found. An approximation for the refractive index for biological material consisting mostly of proteins, which yeast cells do, is the product of the refractive index increment for proteins and the concentration of macromolecules in the cell:

$$n \approx 1.33 + dn/dc \cdot C \approx 1.33 + 0.18 \text{ mL g}^{-1} \cdot 0.40 \text{ g mL}^{-1} \approx 1.40. \quad (4.1)$$

The fact that this approximate value is in the range of the measured values in this experiment, strengthens the reliability of the DHM.

4.2 Yeast cells in optical trapping microscope

The same type of cells were also put in the trapping microscope, see figure 4.2, where a single cell is trapped. One can see from the difference in focus that the trapped cell is not in the same plane as most other cells and by moving the sample, the trapped cell will not move. Figures showing the linear relation between detector voltage and particle position relative to the trap can be seen in figures 4.3a and 4.3b. When calibrating the cell as described in section 3.2.2, the cells were moved at a velocity $v = 34.3 \mu\text{m/s}$, and the average distance between the trap center and cell center $\delta = 485 \text{ nm}$; this can be seen in figure 4.3c. According to equation (4.2), the trapping constant can thus be computed to

$$k_x = \frac{6\pi\eta r v}{-x} = 2.57 \mu\text{N/m}, \quad (4.2)$$

where the cell radius $r = 1.78 \mu\text{m}$ and $\eta = 1.001 \text{ mPa s}$ is the viscosity for water at 20°C [17].

The same calibration were done for a perpendicular direction, vertically in figure 4.2. The result of that calibration were a trapping constant $k_y = 3.42 \mu\text{N/m}$.

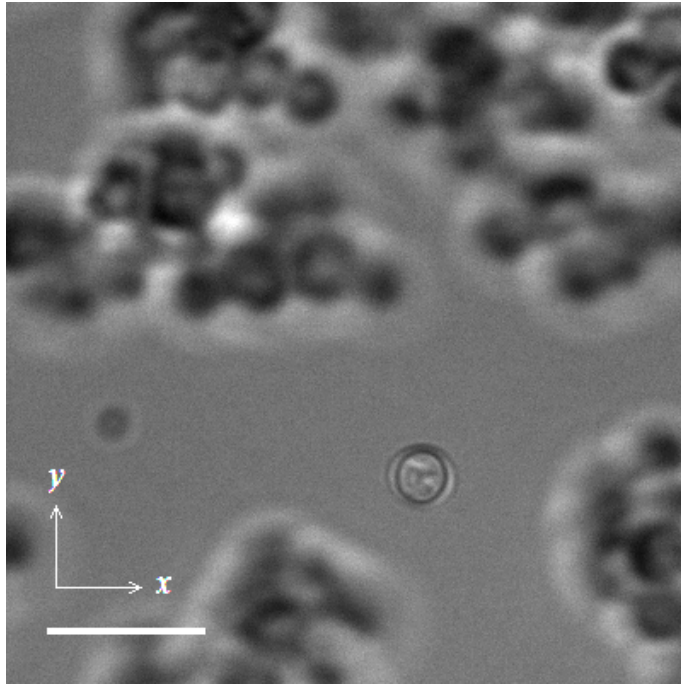


Figure 4.2: *The image of the cells as seen in the OTM, with a single cell captured. The scalebar is 10 μm .*

4.2.1 Discussion

The fact that the trapping strength is quite asymmetric regarding the different directions of calibration can be because of slight difference in focus, since the optical setup is not completely symmetrical. It makes the microscope less versatile, considering that the microscope would have to be calibrated in the specific direction it will later be used. Another setup that does not use mirrors in the same extension as this setup may reduce or remove the difference.

When the IR filter was removed and the beam could be viewed in the camera, it could easily be seen that the beam had two small foci just above and below the main focus at the same plane. This could be another reason why the calibration results differed so much between x and y direction. The first calibration was therefore judged as more reliable and was used for the following experiments.

A hypothesis explaining the low trapping strength, compared to the beads described in the next section, may be that the trap is not holding the entire cell, but an organelle or part of the cell [22]. Since the trap has its strongest intensity in an approximately $1 \mu\text{m}^3$ volume, this is significantly smaller than the cell, see table 4.1.

Note that the calculated trapping strengths are varying with the size and refractive index of the cells, the viscosity and refractive index of the medium and the power and focus of the laser [14]. Since the cells are living and growing, the size and refractive index of the cells will also slowly change with time when they grow or bud off, even though the budding process normally takes a couple of hours.

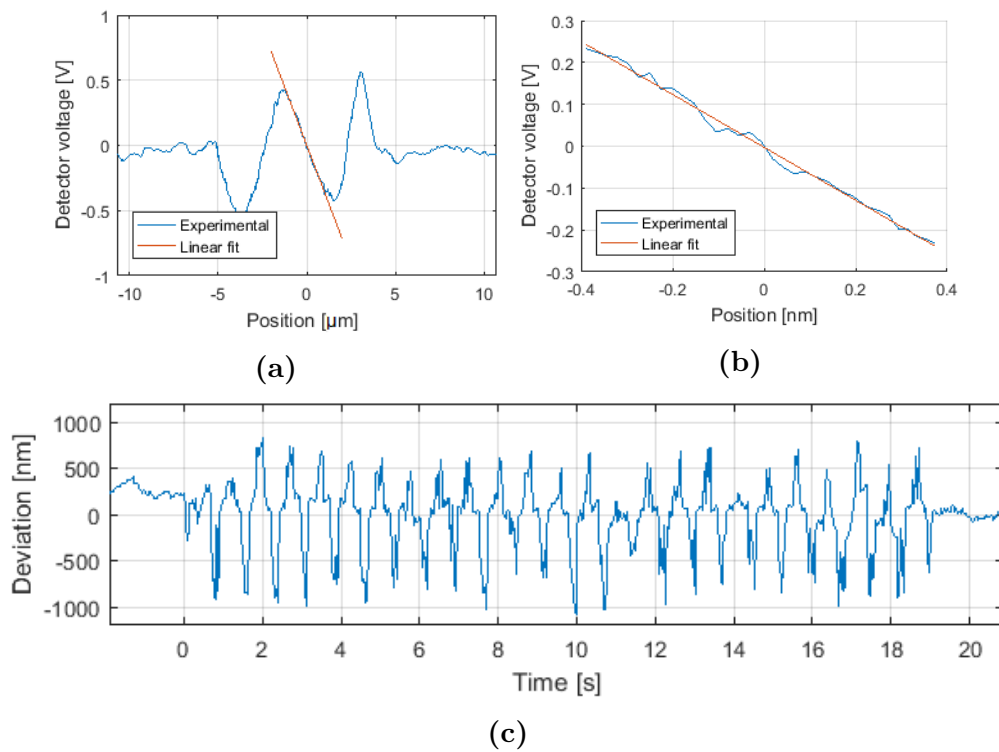


Figure 4.3: (a) By scanning over a fixed cell and registering the voltage response of the detector this correlation is detected. In a close distance to the center of the cell, the relation between voltage response and position is approximated by a linear fit. (b) The sensitivity ρ is calculated from the slope of the linear fit. (c) The deviation of the cell from the trap center as a function of time when using the Stokes drag calibration method.

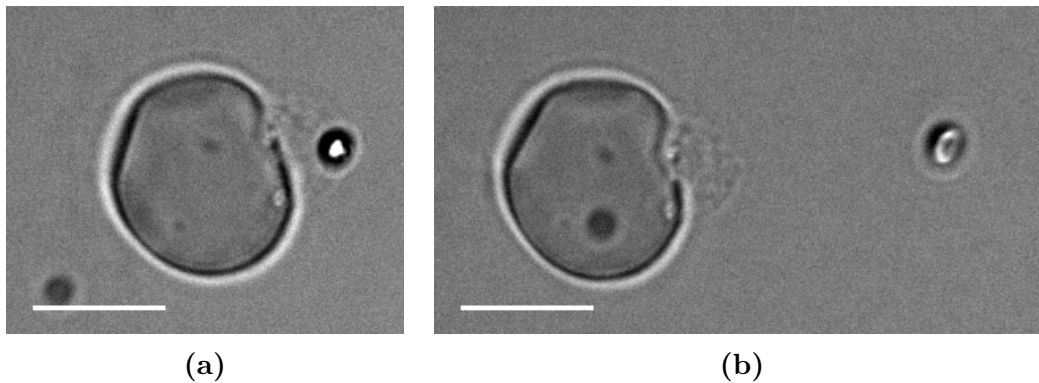


Figure 4.4: *Image of the MLV, GUV and bead. Since the GUV only consists of a single or a few lipid bilayers, it is not possible to resolve in this optical microscope. The scalebars are $10\ \mu\text{m}$. (a) The non-trapped bead stuck on the side of the GUV (b) The bead is pulled $14\ \mu\text{m}$, creating a membrane tube between bead and GUV.*

No further measurements have been done on the yeast cell, but this serves as evidence that cells are easy to manipulate, even though the cells are too large for optimal trapping in this microscope. By comparing with the results from the calibration of $2\ \mu\text{m}$ beads in the next section, it can be seen that the cell is slower to react to movements of the trap, because of its larger size. This can also be seen in the much lower trapping constant.

4.3 Model cells in optical trapping microscope

The main barrier for creating tethers from the cell is the cell membrane. It is one of the largest and most complex organelle of the cell, and a vital part of keeping the cell healthy. It does not only hold proteins that enables communication between the inside of the cell and the outside, but have also been suggested for intercellular communication [9]. The results here presented are one way of characterizing the dynamics of the cell membrane.

Since the basis of the trapping microscope is an optical microscope, the contrast comes from absorption and transmission of light. Considering that the GUVs have a very thin shell, they are sometimes but not always visible in the microscope. Except for seeing the GUV itself, one can also recognize a deformation of the MLV it is grown from. A visible GUV, as in figure 4.4a, may be a sign that it is not a true GUV with a membrane consisting of one single lipid bilayer, but instead comprising of a few layers [28].

In figure 4.4b, the bead on the GUV has been pulled out and a membrane tube created. The membrane tubes generally have a diameter below $100\ \text{nm}$ [29], which is far below the resolution limit of the optical microscope. Even though the tube cannot be resolved in these pictures, watching the video footage clearly shows ev-

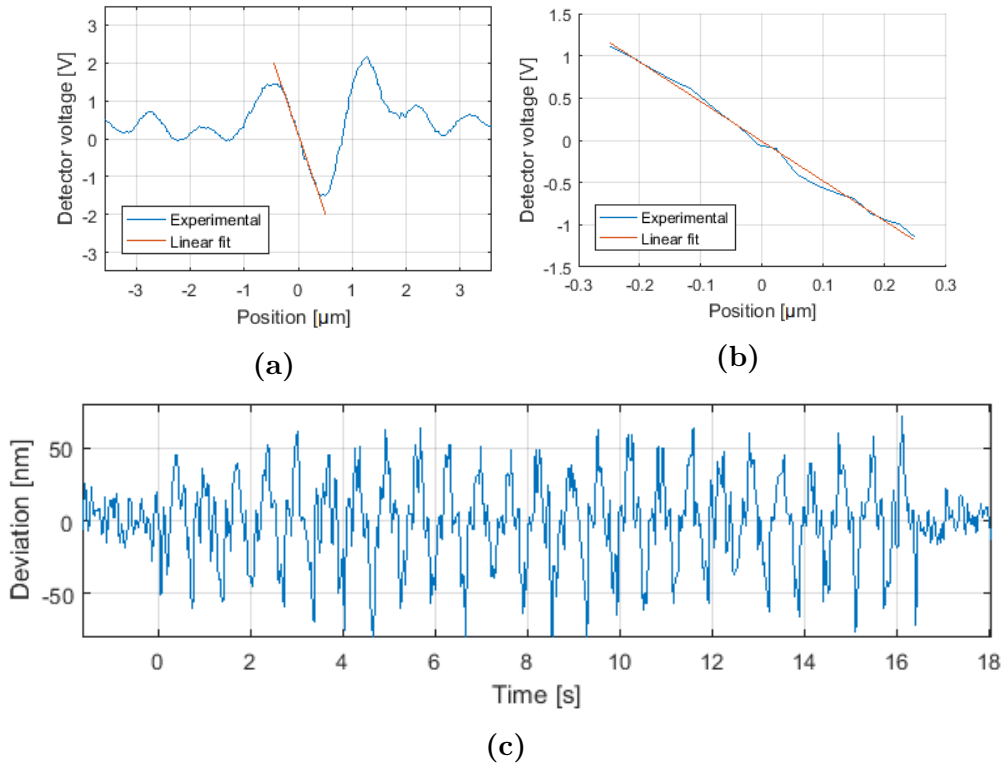


Figure 4.5: (a) Voltage response to scanning over a fixed $2 \mu\text{m}$ bead. (b) The sensitivity ρ is calculated from the slope of the linear fit. (c) The deviation of the bead from the trap center as a function of time when using the Stokes drag calibration method.

idence of a string between the bead and the GUV. When the bead is released it will immediately return to the surface of the GUV. One can also see that the GUV is slightly deformed when a membrane tube is pulled out, at just the spot where the bead previously were. The MLV in the figures 4.4a and 4.4b has a diameter of $14.5 \mu\text{m}$, the membrane tube has a length of $14.0 \mu\text{m}$, and the beads are $2.0 \mu\text{m}$ in diameter. The viscosity of the buffer at 20°C is $1.64 \text{ mPa}\cdot\text{s}$ [5].

Calibration of the beads were made in the same way as for cells, with the results in figures 4.5a - 4.5c; the sensitivity was measured to $\rho = -226 \text{ nm/V}$, and the trapping constant $k = 32.7 \mu\text{N/m}$. This was computed as an average of 3 and 4 measurements respectively. The translation stage holding the cells could not perform automated movements fast enough to find the maximum trapping force. To get an estimation of the maximum force, manual movement of the cell were performed, and a rough approximation of the maximum velocity, before the bead is lost, gotten from analyzing the video footage is $250 \mu\text{m/s}$, which corresponds to a maximum trapping force of approximately 8 pN .

The force profiles from pulling membrane tubes at different velocities can be seen in figures 4.6a - 4.6d. In all figures, three distinct phases can be seen. There is a part with a high force, around 1.5 pN , being exerted on the bead from the GUV, and that

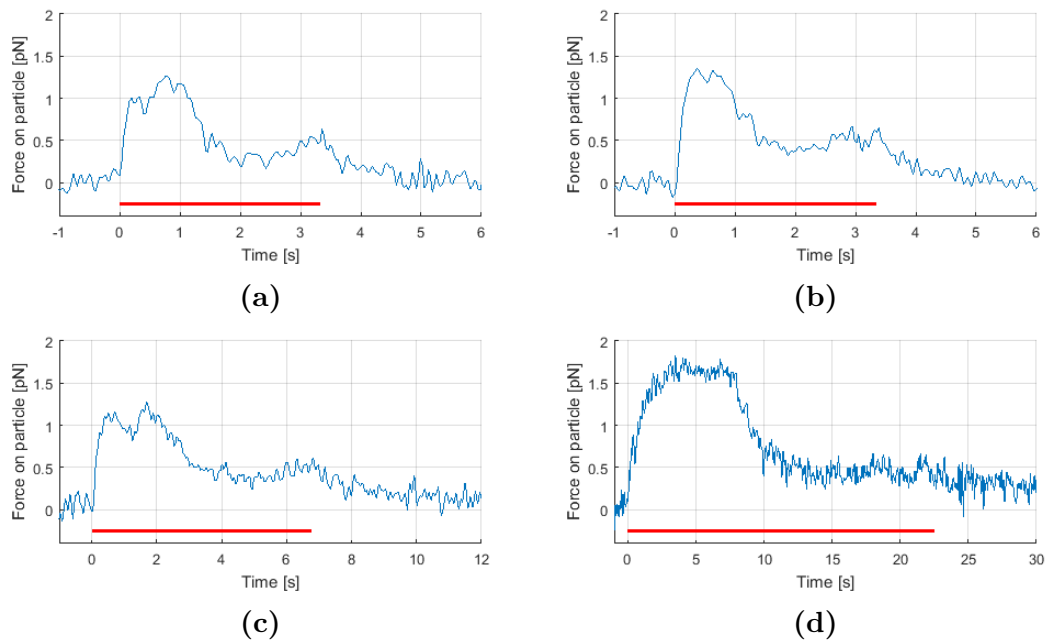


Figure 4.6: Force profile from creating $14 \mu\text{m}$ tethers in the model cell. The red bar indicates for how long the bead was in movement,

- (a) Pulling for 3.3 seconds, using an average of 6 measurements.
- (b) Pulling for 3.3 seconds, using an average of 9 measurements.
- (c) Pulling for 6.8 seconds, using an average of 5 measurements.
- (d) Pulling for 22.5 seconds, using an average of 4 measurements.

is before the tube is created. Then comes a part where the tube is extended, around 0.5-0.75 pN. Lastly there's a relaxing part when the bead is no longer moving. The red bar in the figures shows for how long the extension was going on.

The difference between the measurements in 4.6a and 4.6b is that the measurements used in 4.6b were done after 4.6c and 4.6d. If there are significant differences between the two, this may be because of development or movement of the vesicles. The measurements for 4.6b were also done using shorter pauses between measurements.

In figure 4.6a and 4.6b, there is a very quick relaxation after the movement has stopped. There seems to be no force required to hold the bead after a couple of seconds in these two measurements. The trend for the lower pulling velocities seems to be that the relaxation is slower. In 4.6d, the movement ends after 22.5 seconds, but the force does only very slowly decline.

Notice that there is a slow increase in pulling force in figures 4.6a - 4.6c after the membrane tube have just been created; it takes more force to prolong the tube the longer it is. Any effect like this is not visible in figure 4.6d.

The maximum force required to exit the membrane is significantly higher for the lowest pulling velocity, 1.83 pN, as seen in figure 4.6d. For the other three, maximum forces are 1.26 pN, 1.35 pN and 1.28 pN respectively.

In two of the measurements used for figure 4.6d, the video recording shows larger pieces of lipid material stuck on the membrane tube, but the material is not resolvable on the video. This may however have effected two of the four samples at this pulling velocity.

Since the beads will experience drag force from the surrounding medium while being moved, the drag force was calculated for each measurement, and deducted from the measured force. The force is proportional to the velocity, see equation (2.10), so this had the biggest effect on the faster attempts, with a maximum of 0.29 pN.

4.3.1 Discussion

There are a few studies that has been done on measuring forces on membrane tethers, but no study was found with premises close enough for a direct comparison. One study of blebbing cells, where the plasma membrane and the cytoskeleton temporarily are separated, were done in 1999, where tethering forces between 16 pN and 8 pN were measured for blebs in a renal cell and melanoma cell respectively [10]. Even though these forces are both significantly higher than the tethering forces between 1.81 pN and 1.16 pN in this experiment, it shows that the values for the model cell are at least comparable to blebs.

The increase in pulling force in figures 4.6a - 4.6c may be because the GUV has a

harder time transporting enough material towards the tube for the higher velocities. For the slowest tether formation, the GUV might be able to satiate the membrane tube with enough material, and therefore exert a lower extension force.

The result in figure 4.6c is an average of five separate measurements. Worth noting may be that the overall force required for each attempt were lower than for the one before. This may be a coincidence, but it may also be that the tension in the GUV was somehow reduced with every creation of the membrane tube. There was a slight tendency for this in the measurements for figure 4.6d as well, but not as clear. Maybe this calls for an even stricter protocol than the one used, but no definitive conclusions can be drawn with this small sample size.

There are a lot of factors that may have affected the results. The system is quite sensitive to vibrations, and placing it on a vibration isolated optical table may reduce noise originating in vibrations from the floor. The vesicles are, just like the cells, continuously growing. The changes are too small to change anything on a shorter timescale, but may vary over the time of the whole experiment. In this case, the GUVs grown for 30 minutes before the experiments began. Changes to the GUVs may also stem from the experiment itself, since the induced membrane tension may affect the membrane. Since the optical microscope has a short depth of field, there may be objects out of focus that disturbs the laser beam but cannot be seen on the video recording.

It was also possible to trap MLVs that weren't stuck to the glass surface, if they were small enough. Vesicles larger than 8 μm in diameter could occasionally be trapped, but with a very low trapping constant.

Membrane tethers has been suggested as a way of cell communication, which would require the cell to internally produce forces stronger than the tether force [9]. Since the motor protein dynein can create forces stronger than 7 pN [11], it is evident that tethers in this model cell could be created by the motor proteins active in the yeast cell.

5

Conclusion

This thesis has described two ways of probing cells and model cells. The experiments using the DHM shows great potential, since it is easy to use and gives good results. An expansion of the DHM experiment described in this thesis would be to keep measuring the refractive index over time while changing the osmotic pressure of the solution around the cell. Several experiments like this has been performed by Daniel Midtvedt, and unpublished results show high accuracy and time resolution. By doing this, the density of the cell may also be determined [4].

To increase the statistical relevance of the force measurements, more data would have to be collected. Since there are a lot of properties of the GUV that affects the final result, several GUVs would have to be analyzed with the same protocol. Unfortunately, the creation of GUVs are spontaneous and cannot be controlled using the method described.

One of the desired properties of the streptavidin-coated beads was a very quick and flexible binding to the biotin in the cells. When working with lipids, there will be free floating lipids, micelles, proteins et cetera, as well as free ions. This can cause screening between the biotin in the vesicles and the streptavidin on the beads, with the streptavidin being satiated with biotin before bonding to the GUV. In one study using this combination, bonding between beads and biological material was created by holding the bead against a cell and waiting for 1-3 seconds [10]. This method was never successfully used in this project, but the bonding instead occurred spontaneously during the vesicle culturing. This would probably be a requirement if further analysis requiring tether creation in different GUVs with specific properties. The method of creating GUVs using electroformation technique could also be used [8].

There are a lot of factors separating the measurements of cells and the model cells, since the yeast cell membrane is not as simple as the model cell's. By experimenting with different types of MLVs, adding a combination of surface modifiers, a more realistic model may be realized. Analysis of the yeast cell without its cell wall by exposing the cell to Zymolyase could also be an alternative [19].

The optical trapping microscope is a very flexible tool with a lot of features. The biggest disadvantage of this setting is the range for automated movements and the low resolution of the optical microscope. If the range of automated movements were larger, further analysis of the membrane could be performed, since a longer tube

would start different processes in the membrane. The tether holding force for longer distances could also be analyzed. A higher resolution of the image would enable analysis of the membrane tube, since visual analysis could be used as a complement to the quantitative data. Fluorescence could also be used, since that heavily increases the visibility of GUVs and membrane tubes [33].

If these different microscopy techniques were combined, more rigorous studies of membrane tubes can be performed. Membrane tubes could be created using optical trapping while a DHM can produce data of the thickness and density of the membrane tube. The DHM could also follow the transportation of material in the tube or between cells, while enabling total control over the environment of the cells.

The studies of optical super-resolution the last decades has greatly expanded the magnifications of biological samples, where electron microscopes is not possible. Hopefully, further explorations into cell probing can follow, complementing high resolution imaging with high accuracy information of cell content and cellular development.

Bibliography

- [1] S. Alexandrov, J. McGrath, H. Subhash, F. Boccafoschi, C. Giannini, and M. Leahy. Novel approach for label free super-resolution imaging in far field. *SCIENTIFIC REPORTS*, 5(1):13274, 2015.
- [2] A. Ashkin. Optical trapping and manipulation of neutral particles using lasers. *Proceedings of the National Academy of Sciences of the United States of America*, 94(10):4853–4860, 1997.
- [3] A. Ashkin and J. M. Dziedzic. Optical trapping and manipulation of viruses and bacteria. *Science*, 235(4795):1517–1520, 1987.
- [4] R. Barer and S. Joseph. Refractometry of living cells. *Journal of Cell Science*, 3(32):399–423, 1954.
- [5] BioWest. *Safety data sheet - HEPES Buffer 1 M*, 8 2015. Available at https://www.biowest.net/media/10180s_anglais__029430400_1210_10082015.pdf, 2017-06-16.
- [6] J. M. Burke, P. K. Sorger, J. G. Albeck, S. L. Spencer, and S. Gaudet. Non-genetic origins of cell-to-cell variability in trail-induced apoptosis. *Nature*, 459(7245):428–432, 2009.
- [7] E. Caplain, J.-M. Ringiard, S. Serfaty, L. Martinez, N. Wilkie-Chancellier, and P. Griesmar. Microrheological monitoring of life cycle of yeast cell *saccharomyces cerevisiae*. pages 1514–1517, 2011.
- [8] D. Cuvelier, I. Derényi, P. Bassereau, and P. Nassoy. Coalescence of membrane tethers: Experiments, theory, and applications. *Biophysical Journal*, 88(4):2714–2726, 2005.
- [9] J. Dai and M. P. Sheetz. Mechanical properties of neuronal growth cone membranes studied by tether formation with laser optical tweezers. *Biophysical Journal*, 68(3):988–996, 1995.
- [10] J. Dai and M. P. Sheetz. Membrane tether formation from blebbing cells. *Biophysical Journal*, 77(6):3363–3370, 1999.
- [11] A. Gennerich, A. P. Carter, S. L. Reck-Peterson, and R. D. Vale. Force-induced bidirectional stepping of cytoplasmic dynein. *Cell*, 131(5):952–965, 2007.
- [12] E. Hecht. *Optics*. Pearson, Harlow, Essex, fourth;pearson new international; edition, 2014.
- [13] F. M. Hochmuth, J. Y. Shao, J. Dai, and M. P. Sheetz. Deformation and flow of membrane into tethers extracted from neuronal growth cones. *Biophysical Journal*, 70(1):358–369, 1996.
- [14] Y. Jun, S. K. Tripathy, B. R. J. Narayanareddy, M. K. Mattson-Hoss, and S. P. Gross. Calibration of optical tweezers for in vivo force measurements: How do different approaches compare? *Biophysical Journal*, 107(6):1474–1484, 2014.

- [15] R. Kasprowicz, R. Suman, and P. O’Toole. Characterising live cell behaviour: Traditional label-free and quantitative phase imaging approaches. *INTERNATIONAL JOURNAL OF BIOCHEMISTRY CELL BIOLOGY*, 84:89–95, 2017.
- [16] T. Kodadek. Protein microarrays: prospects and problems. *Chemistry Biology*, 8(2):105–115, 2001.
- [17] D. R. Lide and Chemical Rubber Company. *CRC handbook of chemistry and physics: Ed. 80, 1999-2000 / a ready-reference book of chemical and physical data*. CRC Press, Cleveland, Ohio, 1999.
- [18] P. Marquet, B. Rappaz, P. J. Magistretti, E. Cuche, Y. Emery, T. Colomb, and C. Depeursinge. Digital holographic microscopy: a noninvasive contrast imaging technique allowing quantitative visualization of living cells with subwavelength axial accuracy. *Optics Letters*, 30(5):468–470, 2005.
- [19] M. C. Munder, D. Midtvedt, T. Franzmann, E. Nuske, O. Otto, M. Herbig, E. Ulbricht, P. Muller, A. Taubenberger, S. Maharana, L. Malinowska, D. Richter, J. Guck, V. Zaburdaev, and S. Alberti. A ph-driven transition of the cytoplasm from a fluid- to a solid-like state promotes entry into dormancy. *ELIFE*, 5(2016), 2016.
- [20] P. Müller, M. Schürmann, and J. Guck. The theory of diffraction tomography. 2015.
- [21] T. A. Nieminen, V. L. Y. Loke, A. B. Stilgoe, G. Knöner, A. M. Brańczyk, N. R. Heckenberg, and H. Rubinsztein-Dunlop. Optical tweezers computational toolbox. *Journal of Optics A: Pure and Applied Optics*, 9(8):S196–S203, 2007.
- [22] K. Norregaard, L. Jauffred, K. Berg-Sørensen, and L. B. Oddershede. Optical manipulation of single molecules in the living cell. *PHYSICAL CHEMISTRY CHEMICAL PHYSICS*, 16(25):12614–12624, 2014.
- [23] F. L. Pedrotti and L. S. Pedrotti. *Introduction to optics*. Prentice-Hall, Englewood Cliffs, N.J, 1987.
- [24] E. J. G. Peterman, F. Gittes, and C. F. Schmidt. Laser-induced heating in optical traps. *Biophysical Journal*, 84(2):1308–1316, 2003.
- [25] Polysciences. *Streptavidin and Biotin Conjugated Microspheres*, 4 2016. Rev 9. Available at <http://www.polysciences.com/skin/frontend/default/polysciences/pdf/TDS%20616.pdf> 2017-06-16.
- [26] J. M. Rodríguez-Peña, V. J. Cid, J. Arroyo, and C. Nombela. A novel family of cell wall-related proteins regulated differently during the yeast life cycle. *Molecular and Cellular Biology*, 20(9):3245–3255, 2000.
- [27] M. Saleemuddin and Q. Husain. Concanavalin A: A useful ligand for glycoenzyme immobilization – a review. *Enzyme and Microbial Technology*, 13(4):290–295, 1991.
- [28] N. Stepanyants. *Lipid Nanotubes as a Model for Highly Curved Cellular Membrane Structures*. PhD thesis, 2013.
- [29] N. Stepanyants, G. D. M. Jeffries, O. Orwar, and A. Jesorka. Radial sizing of lipid nanotubes using membrane displacement analysis. *Nano Letters*, 12(3):1372–1378, 2012.

-
- [30] Y. S. Sun, J. P. Landry, Y. Y. Fei, X. D. Zhu, J. T. Luo, X. B. Wang, and K. S. Lam. Effect of fluorescently labeling protein probes on kinetics of protein-ligand reactions. *Langmuir*, 24(23):13399–13405, 2008.
- [31] Thorlabs. *Optical trap kit*, 4 2012. Available at http://res.abtronics.ru/pdf/479/968/754/abtronics_OTKB_0.pdf 2017-06-07.
- [32] Thorlabs. *Optical Trap Kit Force Module*, 11 2014. Available at <https://www.thorlabs.com/drawings/89dcd7dda279efae-18723DBE-E2F0-1266-943DF7426F3867EB/OTKBFM-Manual.pdf> 2017-06-07.
- [33] I. Wegrzyn, H. Zhang, O. Orwar, and A. Jesorka. Nanotube-interconnected liposome networks. *Nano Communication Networks*, 2(1):4–15, 2011.
- [34] Z. Zalevsky, D. Mendlovic, SpringerLink, and A. SpringerLink. *Optical Super-resolution*, volume 91. Springer New York, New York, NY, 2004.
- [35] F. Zernike. Phase contrast, a new method for the microscopic observation of transparent objects. *Physica*, 9(7):686–698, 1942.
- [36] F. Zernike. Phase contrast, a new method for the microscopic observation of transparent objects part ii. *Physica*, 9(10):974,IN1,981,IN3,983–980,IN1,982,IN3,986, 1942.
- [37] H. Zhang and K.-K. Liu. Optical tweezers for single cells. *Journal of The Royal Society Interface*, 5(24):671–690, 2008.